Ferromagnetism in ion implanted amorphous and nanocrystalline Mn$_x$Ge$_{1-x}$

A. Verna,[*] L. Ottaviano, M. Passacantando, S. Santucci, P. Picozzi, F. D'Orazio, and F. Lucari
Dipartimento di Fisica, Università di L'Aquila, Via Vetoio 10, I-67010 Coppito, L'Aquila, Italy

M. De Biase
Via Madonna Fore 23, I-67100 L'Aquila, Italy

R. Gunnella
Dipartimento di Fisica, Università di Camerino, Via Madonna delle Carceri, I-62032 Camerino (MC), Italy

M. Berti and A. Gasparotto
MATIS-CNR-INFM and Dipartimento di Fisica, Università di Padova, Via Marzolo 8, I-35131 Padova, Italy

G. Impellizzeri and F. Priolo
MATIS-CNR-INFM and Dipartimento di Fisica, Università di Catania, Via S. Sofia 64, I-95123 Catania, Italy

The structural, electronic, and magnetic properties of a Mn$_x$Ge$_{1-x}$ alloy prepared through room-temperature ion implantation (100 keV, 2×10^{16} ions/cm^2) and subsequent 400 °C annealing have been investigated with several experimental techniques. The as-implanted sample shows a quasi-Gaussian Mn concentration depth profile with a projected range (peak Mn concentration $x \simeq 12$ at./%) at 55 nm and end of range at 140 nm. The structural investigation shows that the overall implanted Ge layer is amorphous. In particular, up to a depth of 60 nm, the implanted layer is also porous and oxidized, whereas the deepest implanted region (60–140 nm) is purely composed of amorphous Ge with Mn atoms diluted in it. This sample manifests magnetic hysteresis up to 20 K and a strong nonlinear S-shaped magnetic response up to 150 K. Upon annealing at 400 °C, the top porous layer remains essentially amorphous, whereas partial reconstruction into Ge nanocrystals ($\sim$10 nm in diameter) occurs in the 60–140-nm-deep implanted region. Part of the Mn atoms, mainly belonging to the top porous layer, further diffuses toward the surface and forms chemical bonds with O contaminants, becoming magnetically inactive. The other Mn atoms, mainly in the region between 60 and 140 nm from the surface, remain trapped in the residual amorphous matrix or in the Ge nanocrystals, whereas formation of Mn-Ge extrinsic phases (like Mn$_{11}$Ge$_8$ and Mn$_5$Ge$_3$) is excluded. The magnetic response of the annealed sample originates from the existence of a soft and a harder magnetic component, assigned to the dilution of Mn atoms in residual amorphous Ge and Ge nanocrystals, respectively. The hard component, attributable to a Mn$_x$Ge$_{1-x}$ diluted magnetic semiconductor in nanocrystalline form, manifests magnetic hysteresis up to above 250 K.

I. INTRODUCTION

The use of materials that possess, at the same time, semiconductive and magnetic properties constitutes one of the most promising research lines in the field of spintronics.[1–5] Magnetic properties can be achieved in the zinc-blende structure semiconductors (conventionally used in microelectronics and optoelectronics) through incorporation of transition-metal (TM) impurities in a diluted phase.[1] This new class of materials, widely referred to as diluted magnetic semiconductors (DMSs), would allow the injection and detection of spin-polarized currents.[1] Moreover, unlike ferromagnetic metals, they allow the control of the concentration and the orientation of charge (and spin) carriers through the simple application of an external bias,[6] or through lighting.[7]

The main issue for a DMS is the effective dilution of the TM magnetic dopants at the highest possible concentration in order to achieve stable and effective magnetic properties and spin-carrier polarization up to a Curie temperatures (T_C) as high as possible. The achievement of critical temperatures above ambient conditions is obviously of fundamental interest for technological applications. However, the request for a dilution of TM atoms at high densities conflicts with the very low solubility limit that nonhydrogenic TM impurities have in III-V and group-IV conventional semiconductors, usually of the order of 10^{18} cm^{-3} even at temperatures around 1000 K,[1,8] whereas concentrations at least around 10^{20} cm^{-3} (few percents of the overall atomic density) are needed to establish ferromagnetism.[1] Therefore, TM impurities tend to form dimers (i.e., couples of nearest-neighbor TM atoms) with total null magnetic moments, or extrinsic precipitates with host matrix elements.[9,10] For this reason, a growth technique that works far from thermodynamical equilibrium is required to achieve effective dilution. Among the several out-of-equilibrium growth techniques, molecular beam epitaxy (MBE) performed at relatively low temperatures [sometimes well below 250 °C (Ref. 1)] has been by far the most used and explored. Starting from the 1990's, most of the theoretical and experimental efforts have been focused on III-V semiconductors, particularly on GaAs.[11] Through Mn δ-doping of AlGaAs/GaAs heterostructures grown by MBE, a T_C up to 250 K has been reached.[12]

In recent years, significant attention has been focused on the theoretical study and experimental realization of group-

IV-based DMS (i.e., Si, Ge, SiGe), for their obvious advantage of a full compatibility with the mainstream silicon technology. In particular, Mn doping of Ge at high concentrations (1–10%) is by far the most promising material.[13] Theoretical works clearly indicate that Mn plays a role in making the doped Ge lattice a ferromagnet, particularly if the doping takes place via Mn substitution of Ge atoms in the lattice. In this case, Mn behaves as a double acceptor impurity in the Ge matrix and the resulting high concentration of holes is responsible for the exchange interaction between the Mn magnetic impurities.[14,15] Mn doping in Ge was first experimentally studied by Woodbury and Tyler[16] in samples prepared through the diffusion technique and so with a very low Mn atomic concentration (estimated around 10^{-6}). They carried out an accurate characterization of the electric response and verified the double acceptor behavior of Mn impurities. However, neither microscopic nor magnetic characterization was given of the material. More recently, Park and co-workers reinvestigated Mn_xGe_{1-x} alloys fabricated at high Mn atomic concentration ($x=0.006 \div 0.035$) by means of MBE, finding Curie temperatures up to 116 K.[17] Many other groups came into the arena of the study of the structural, electronic, and magnetic properties of MBE fabricated MnGe alloys: as a result, a quite systematic collection of experimental data is now at hand as a function of Mn concentration and Ge substrate temperature during the MBE growth (see, for example, Refs. 18–20). Co-doping with Co has been also explored,[21] as well as doping with magnetic atoms other than Mn (such as Cr in Ref. 22). From all these studies, it appears evident that homogeneous dilution of Mn in the Ge lattice by MBE is really difficult to achieve. Typically, when a relatively high substrate temperature is used during MBE growth (200–300 °C), Mn atoms precipitate into very stable Mn rich metallic clusters such as $Mn_{11}Ge_8$ or Mn_5Ge_3. These clusters, ferromagnetic at room temperature, are trivially responsible for the claimed room temperature (or above) ferromagnetism of many MnGe alloys.[10,23]

An alternative and very promising nonequilibrium technique for the fabrication of DMS is given by the ion implantation of TM species. This method has been carried out typically for III-V semiconductors [GaAs,[24] InP,[25] GaN,[26–28] GaP (Refs. 28 and 29)], and recently in the case of SiC (Refs. 28 and 30) and Si.[31] Room-temperature ion implantation of Mn in Ge has been performed by L. Liu and co-workers[32,33] verifying the presence of ferromagnetic response but with little further work. Our group has focused its attention on a systematic study of the effects of ion implantation parameters (dose and Ge substrate temperature) on the structural and electronic properties of the ion-implanted Mn-Ge alloys, and their influence on the magnetic response of the Mn-doped thin film. Recently, for Mn ions implanted in Ge substrates kept at 300 °C, we have reported the coexistence of dilution in the Ge crystalline matrix and phase separation into Mn-rich clusters.[34,35] The density, size, and crystalline quality of these Mn-rich precipitates increases with the implanted dose, and metallic Mn_5Ge_3 clusters are obtained for the higher dose rates. Mn_5Ge_3 precipitates dominate the magnetic properties of the samples, which manifest T_C up to 270 K.[35] The same coexistence of dilution and phase separation has also been verified in MBE-grown MnGe alloys.[36] Here we focus

on Ge wafers implanted with Mn ions at room temperature (RT), which is the lowest limit of investigated temperatures. For these samples, after annealing at 400 °C, dilution of Mn atoms has already been demonstrated by x-ray absorption spectroscopy measurements and their comparison with first-principle calculations.[37] In the present work we perform a comprehensive analysis of the structural and electronic properties of RT Mn ion implantation in Ge, and we correlate these characteristics with the observed magnetic response. Many different experimental techniques have been employed in order to ensure a cross-check of the obtained information and to illustrate a complete as possible picture of the phenomena that occurred. The morphology of the sample surface, as altered by the ion implantation process, has been analyzed through atomic force microscopy (AFM). Channeling Rutherford backscattering spectrometry (c-RBS), transmission electron microscopy (TEM), and diffraction by x-rays and electrons have been employed to study the structural properties of the implanted host Ge matrix and its crystalline quality. Elemental depth profile composition has been obtained by core-level x-ray photoemission spectroscopy (XPS) and electron dispersive analysis of x-rays (EDAX). Besides, soft x-ray photoemission has been employed to investigate the density of states in valence band. Finally, the magnetic response of the samples has been studied through magneto-optical Kerr effect (MOKE), assuming a proportionality between the magnetization M in the sample and the rotation θ of the polarization plane.[38]

As we shall see, RT ion implantation produces a completely amorphous host Ge layer with Mn atoms diluted in it, with poor magnetic properties and a T_C estimated around 20 K. Upon annealing at moderate temperature (400 °C), a layer of nanometric Ge crystallites is produced with significant incorporation of Mn atoms (average atomic concentration x around 6%), and total absence of Mn-rich metallic precipitates. The magnetic response of such a polycrystalline Mn-Ge alloy exhibits T_C above 250 °C, which is remarkably high compared to the ones reported at similar x values in MBE-grown samples.

II. EXPERIMENTAL

(001)-oriented *n*-type Czochralski (CZ) Ge wafers, with a nominal resistivity 10^{-3}–10^{-2} Ω cm, have been implanted with 100 keV Mn^+ ions with a dose of 2×10^{16} ions/cm². The substrate has been maintained at room temperature during the implantation process, with the [001] axis forming an angle of 7° with respect to the impinging beam direction, in order to avoid channeling phenomena. From TRIM Monte Carlo simulation,[39] the expected projected range R_p (i.e., the depth of maximum concentration) for Mn ions at the chosen beam energy is ~55 nm and the end of the implantation range is situated at ~140 nm. Portions of the implanted wafers have been subsequently annealed for 1 h in ultrahigh vacuum (pressure ~10^{-8} Pa) at temperatures ranging from 50 to 400 °C.

Tapping mode AFM measurements have been performed *ex situ* in air with a Digital Dimension D5000 instrument equipped with a Nanoscope IV controller, using a Si cantile-

ver (300 kHz resonance frequency). c-RBS measurements have been carried out at the 7 MV-Van de Graaff CN Accelerator of the INFN Legnaro National Laboratories, using as a probe a highly collimated beam of He$^+$ ions, accelerated at $E_0 = 2.2$ MeV; backscattered particles are revealed with the detector placed at 170° with respect to the incident beam direction. Measurements have been carried out in alignment conditions along [001] direction and in rotating random configuration. Cross-sectional TEM, electron diffraction, and EDAX measurements have been carried out using a Philips CM200 microscope. X-ray diffraction (XRD) measurements have been performed in grazing incidence geometry (incident angle of 1.0°) using a Siemens D-5000 diffractometer, equipped with a Cu anode and a solid state detector for scattered x-rays. A Göbel mirror is used to collimate the incident x-ray beam and to select the Cu $K\alpha$ emission line ($K\alpha_1$ $\lambda = 1.5406$ Å, $K\alpha_2$ $\lambda = 1.5444$ Å). The background signal for low 2θ angles has been subtracted using a standard algorithm. The wafers have been oriented in order to exclude the presence of very intense diffraction peaks due to monocrystalline Ge substrate. An ESCA PHI 1257 apparatus has been used for standard x-ray photoemission spectroscopy. Depth profiles of implanted Mn impurities, host Ge atoms, and other possible contaminants are obtained through a progressive *in situ* sputtering by Ar$^+$ ions (2 keV, 45° incidence with respect to the sample surface, 1.8 nm/min etch rate[40]). A stoichiometric Mn_5Ge_3 thin film grown by MBE on Ge (111) (Ref. [41]) has been used as standard for absolute calibration of a relative Mn/Ge cross section. Valence-band photoemission spectra have been measured at the vuv beamline[42] of ELETTRA synchrotron radiation facility in Trieste, using the following settings: radiation energy of $h\nu = 120$ eV, normal emission mode, detector angular acceptance of 7°, and a resolution energy of 20 meV. MOKE measurements have been collected in the temperature range from 10 to 300 K. Infrared radiation ($\lambda = 2.00$ μm) incident on the sample at an angle of 45° with s-polarization has been used as a probe. This wavelength has been chosen because it is just above the Ge absorbing edge and so it allows a suitable penetration inside the sample, much larger than the end of range of the implanted layer. Hysteresis loops have been obtained by varying the applied magnetic field in the range ±5600 Oe; both polar and longitudinal geometry have been explored.[38]

III. RESULTS

A. Structural and electronic properties

Figure 1 reports the obtained AFM micrographs for as-implanted and 400 °C annealed samples, together with the corresponding height line profiles, taken on the indicated paths. The high roughness of the surface in both samples is clearly verified, the difference in height between highest peaks and deepest valleys being about 35–40 nm. Height histograms, not reported, show for both samples a Gaussian-type distribution, with a FWHM of ~14 nm, which can be assumed as an estimate of the surface roughness. The cobblestonelike morphology of the surface is pointed out also in the bright field plan-view TEM image, shown in the inset of Fig. 1(b). The presence of a significant roughness is typical of a
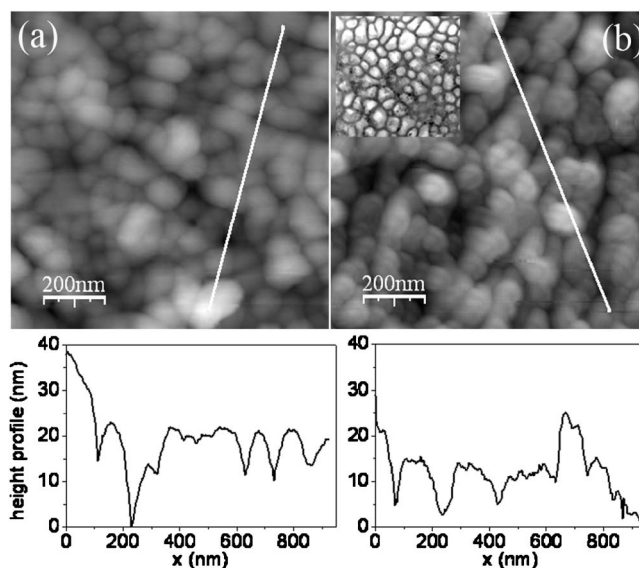

FIG. 1. AFM micrographs of (a) as-implanted sample and (b) sample annealed at 400 °C. The corresponding height line profiles taken along the white lines in the micrographs are reported below. Inset in (b): bright field plan-view TEM image of the annealed sample (1×1 μm area).

high-dose ion implantation process and it is generally an indication that a high degree of crystalline disorder, at worst amorphization, occurred in the implanted layer due to collisional cascades. The highly disordered material has an average lattice parameter greater than the one of the unimplanted crystalline substrate. This turns out in a swelling of the material and in an increased roughening of the surface, as it has been verified for Ge (Ref. [43]) and many other semiconductive targets (see, for example, Refs. [44–46]). A 400 °C annealing process has no significant effect on surface morphology, the degree of roughness remaining unchanged.

In Fig. 2 we report the [001] c-RBS spectra for the as-implanted and the annealed samples in comparison with the random spectrum for the as-implanted sample. A similar spectrum is also found for the 400 °C annealed sample. [001]-aligned and random spectra taken on a pure Ge CZ wafer are also shown for comparison. Two main results can be inferred from the obtained spectra. First of all, in random configuration, around the Ge backscattering edge ($K_{Ge}E_0 = 1767$ keV) and at lower energy down to ~1710 keV, the Ge backscattering signal of the as-implanted sample is distinctly lower than in the pure Ge reference. This is an obvious consequence of the fact that near the surface not only Ge but also implanted Mn atoms are present; moreover, as it will be shown in the following, oxygen contaminants are also present in the implanted layer. Anyway, the backscattering signal from Mn atoms below the edge $K_{Mn}E_0 = 1647$ keV is masked by the yield of the heavier Ge host element. Most importantly, approximately in the same energy range where the signal of the random spectrum is lower than the Ge reference, the as-implanted and 400 °C annealed samples present a peak in the [001] channeling yield, indicating a very high degree of disorder in the implanted layer.[47] For lower backscattering energies, the ratio between the channel-
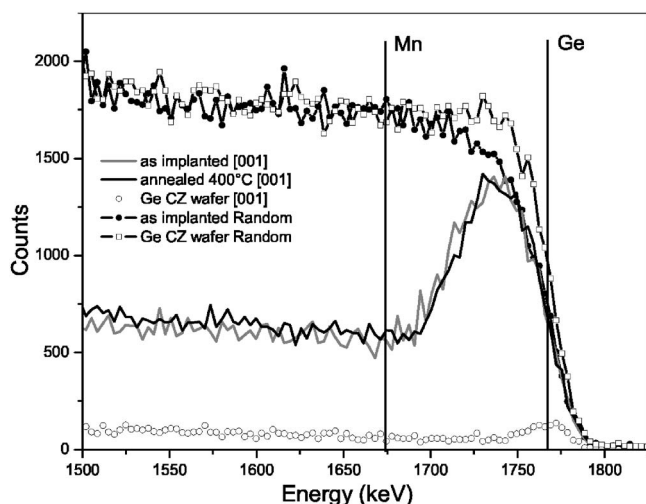
FIG. 2. [001] c-RBS spectra for as-implanted Mn_xGe_{1-x} (gray solid line), 400 °C annealed (black solid line), single crystal CZ Ge(001) (circles). Rotating random spectra of as-implanted sample (full dots) and single crystal (100) CZ Ge (empty squares). Counts are normalized to 10 μC of incident charge and 1 millisteradian of detector solid angle. Backscattering edge for Mn (1647 keV) and for Ge (1767 keV) are shown.

ing and the random RBS signal remains constant, indicating that, below the near-to-surface highly damaged layer, a good crystalline quality region is present. The strong increase in channeling yield, with respect to the unimplanted Ge reference also in this region, is due to the dechanneling of incident He$^+$ ions that takes place in the near-surface defective zone. The FWHM of the surface channeling peak, calculated taking into account the dechanneling contribution to c-RBS yield for the lower-energy side of the peak,[47] amounts to ~55 keV. Assuming a stopping cross section and a density equal to that of pure crystalline Ge (4.41×10^{22} at./cm^3), the corresponding thickness for the highly damaged layer is ~90 nm. Nevertheless, two main factors can significantly increase this estimate. Indeed, the significant presence of elements lighter than Ge, such as Mn and O, reduces the ion stopping power. Moreover, an amorphous, or in any case, highly damaged Ge layer is also expected to have a significantly lower density (up to 25%) than the crystalline phase,[48] the same lower density being responsible for the roughening of the surface verified by AFM measurements, as it has been already pointed out. Likely, these effects lead to a thickness of the highly damaged region very close to the end of range of the implantation estimated by TRIM simulation (140 nm). No significant differences between as-implanted and annealed channeling spectra are evident. This indicates that 400 °C conventional thermal annealing has not induced an epitaxial reconstruction of the implanted damaged layer.

A TEM cross section of the as-implanted sample is shown in Fig. 3(a), together with the EDAX spectra taken at two different depths (marked by the squared regions in the figure). The high roughening of the surface, already indicated by AFM measurements, can be observed. From the obtained image, three different regions can be clearly distinguished. An upper region, extending from the surface to about 60 nm
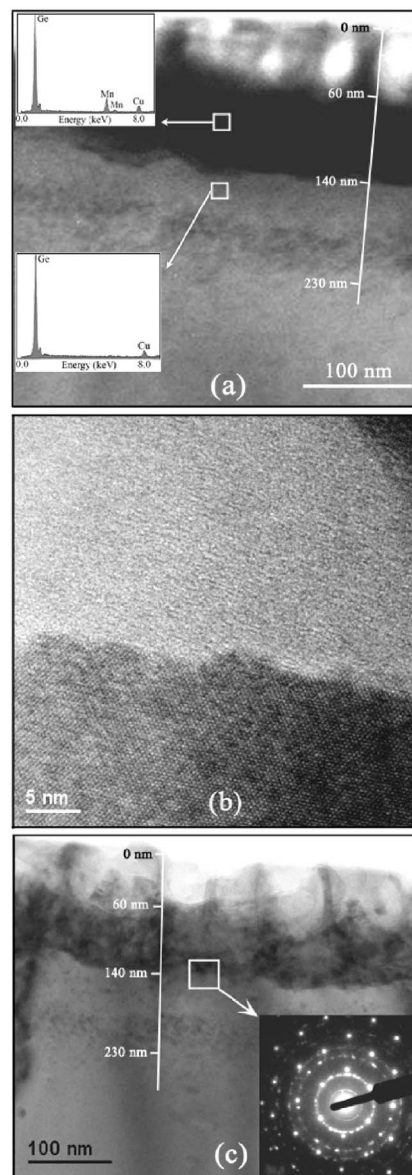

FIG. 3. (a) TEM cross section of the as-implanted sample. Insets: EDAX spectra taken on the two squared regions. Characteristic Cu emission lines in the spectra are due to the copper grid. (b) Atomic resolution magnification of the interfacial zone between the amorphous implanted layer and the single crystalline substrate, in the same cross-sectioned specimen of panel (a). (c) TEM cross section of the 400 °C annealed sample. Inset: electron-diffraction pattern taken on the squared region in the image.

depth, shows an indented structure with vertical channels. These channels separate structures with a lighter gray color. The second region extends from 60 to 140 nm and presents a homogeneous darker contrast well distinguishable from the lower substrate region. In the substrate layer, however, dark contrast spots are present up to a depth of ~230 nm, immersed in the lighter matrix. The same three layered structures have been found in the past in Ge and compound semiconductor samples processed with room-temperature high-dose ion implantation.[44,49,50] The indentationlike structures in the top part (~60 nm) of the implanted layer have been al-

ready shown in literature[49] and they are assigned to the formation of a thin porous film, a phenomenon that in many (but not all) semiconductor targets usually accompanies the amorphization and swelling of the implanted layer,[44,49,50] and that has recently attracted attention for possible technological applications. The porosity of the first 60 nm can explain the presence in this region of oxygen atoms as contaminants, as verified by XPS measurements (see below).

The interface at 140 nm likely corresponds to the end of range of Mn ions and to the boundary between the implanted and unimplanted layer. In fact, the EDAX spectra reveal the presence of implanted Mn atoms only in the first 130–140 nm [as proved by the $K\alpha$ and $K\beta$ emission lines in the upper inset of Fig. 3(a)], whereas no trace of Mn is present immediately below the interface [lower inset of Fig. 3(a)]. A high-resolution cross-sectional TEM image taken across the 140 nm interface is shown in Fig. 3(b). In the deeper region a crystalline order is clearly evinced, whereas atoms appear distributed in a disordered way in the layer nearer to the surface. This indicates that the ion implantation caused the amorphization of the processed layer up to a depth of about 140 nm, corresponding to the end of range of Mn atoms, while the good monocrystalline quality of the substrate below is maintained. This picture is consistent with the c-RBS measurements, taking into account the underestimate of the amorphous layer thickness, as discussed above. Dark spots in the substrate region, present up to ∼230 nm from the surface, represent extended defects formed by the coalescence of excess Ge interstitials generated by the high-dose ion implantation process. Electron-diffraction measurements, not shown, reveal the presence of well-defined diffraction Ge spots in the crystalline substrate, whereas only diffuse scattering can be found in the amorphous implanted layer.

Figure 3(c) reports a TEM cross section of the sample after 400 °C annealing. The same three-layered structure is observed also in this case, indicating that no epitaxial regrowth occurred as a consequence of the annealing procedure. However, in the 60–140-nm-deep layer a granular structure is clearly evident, in place of the homogeneous dark contrast observed for the as-implanted sample [Fig. 3(a)]. Granular structures barely appear also in the top porous layer in the 30–60-nm-deep region. Electron diffraction measurement has been carried out across the interface between the monocrystalline substrate and the implanted region and is reported in the inset. It shows the diffraction spots assigned to the crystalline Ge substrate, superimposed to diffraction rings with the same exchanged momentum $|\Delta\mathbf{k}|$, indicating the presence of Ge polycrystallites in the implanted layer.[51] Evidently, these Ge crystallites formed upon the annealing at 400 °C by reconstruction of the initially amorphous implanted layer. According to the literature, annealing at 400 °C should be sufficient for an epitaxial reconstruction of the amorphous Ge implanted layer[52] (whereas higher temperatures are requested for solid phase epitaxy in the Si case), but this process is probably inhibited by the Mn doping or by the considerable amount of extended defects due to excess interstitials below the end of range. Diffuse electron scattering in the image also proves the presence of nonreconstructed amorphous Ge regions between the Ge nanocrystal-
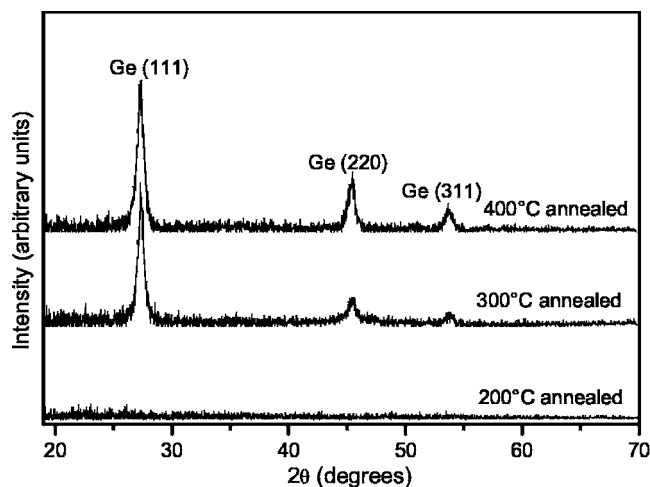

FIG. 4. Grazing incidence (1°) XRD spectra for samples annealed for 1 h at different temperatures: 200 °C (bottom), 300 °C (center), and 400 °C (top).

lites. No diffraction patterns other than those relative to Ge zinc-blende crystal are present. The formation of a polycrystalline layer explains the granular appearance in the deepest region of the implanted layer and the absence of variations in channeling-RBS yields between the as-implanted and the 400 °C annealed sample (Fig. 2), since random-oriented crystallites obviously cannot allow the channeling of impinging ions. From the TEM image [Fig. 3(c)] we verify that the polycrystalline reconstruction of the amorphous implanted layer takes place principally in the region at 60–140 nm from the surface. Only at few crystallites appear in the top (0–60 nm implantation depth range) swelled, porous, and oxidized (see below) layer, that essentially remains amorphous.

The transition from the amorphous to the polycrystalline phase of the Mn-implanted Ge layer is also confirmed by grazing incidence XRD measurements shown in Fig. 4, where the spectra obtained for three different annealing temperatures (200, 300, and 400 °C) are shown. As it can be evinced, the transition takes place in the annealing temperature range between 200 and 300 °C. In the as-implanted (not shown) and 200 °C annealed sample no diffraction peaks are observed; after 300 and 400 °C annealing lines corresponding to Ge (111); $\theta=27.28°$, (220); $2\theta=45.30°$, and (311); $2\theta=53.68°$ diffraction are a clear indication of polycrystallinity. As in the case of electron-diffraction measurements, no peaks relative to Mn-Ge rich precipitates are present. On the contrary, in samples prepared by high-temperature ion implantation, the presence of Mn_5Ge_3 precipitates are distinctly indicated by x-ray diffraction patterns [for example, by the (002) Mn_5Ge_3 peak at 35.45° shown in Ref. 34]. The width of the diffraction peaks can be used to estimate the average dimension of Ge nanocrystals through the Scherrer formula:[53] in the 400 °C annealed sample, the FWHM of the Ge (111) diffraction peak results are 0.73°, corresponding to an average Ge grain size of ∼11 nm.[54]

The results of the XPS depth profiling analysis for the as-implanted and 400 °C annealed sample are summarized in Fig. 5. The obtained Mn $2p_{3/2}$, Ge $3d$, and O $1s$ XPS
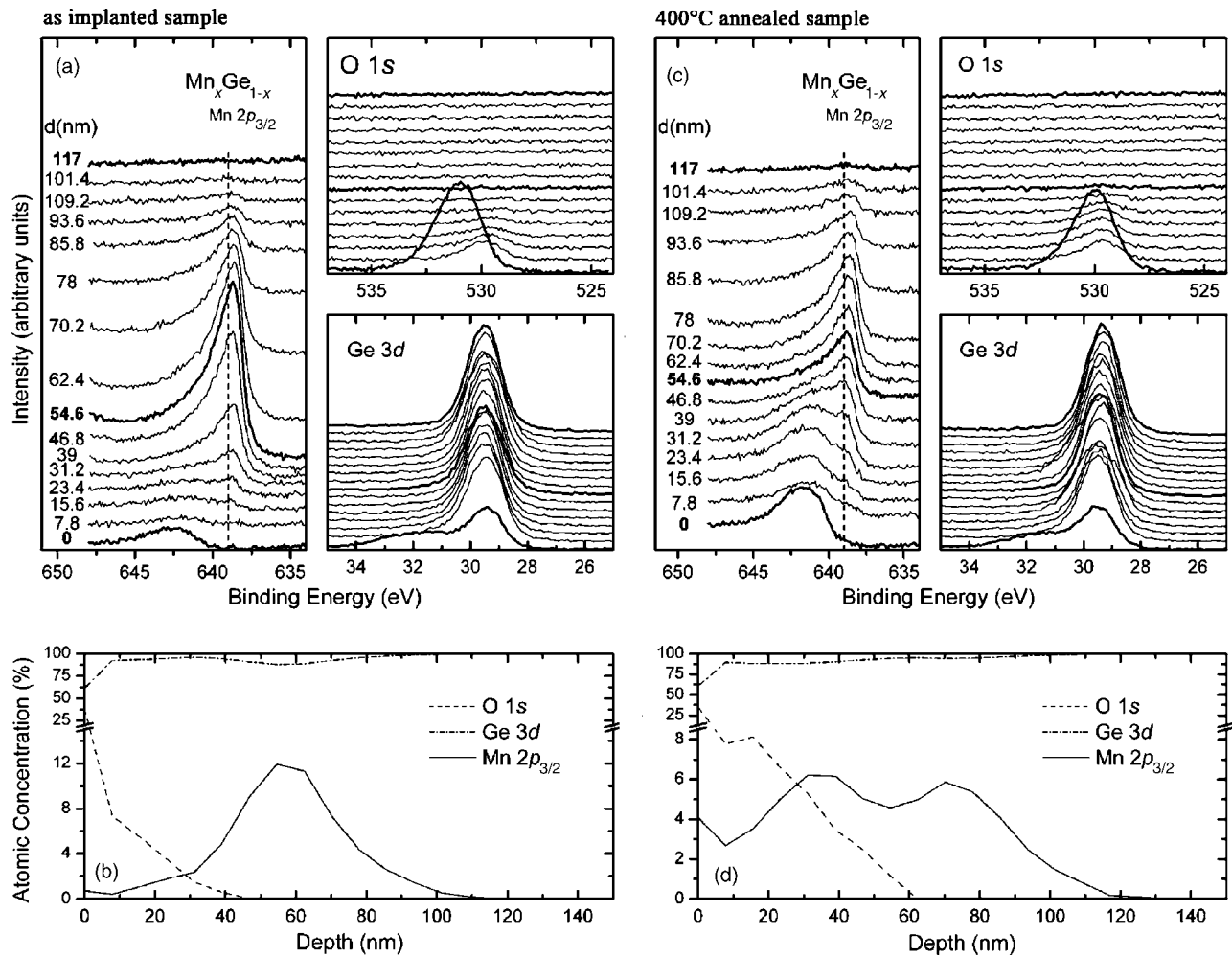
FIG. 5. XPS depth profile analysis of the as-implanted and 400 °C annealed sample. (a), (c) Mn $2p_{3/2}$, Ge $3d$, and O $1s$ core level spectra as a function of reported sputtering depth d (nm) for as-implanted and annealed samples, respectively. Dashed vertical lines in the Mn $2p_{3/2}$ panel indicate the peak position for pure metallic Mn at 639.0 eV. (b), (d) Concentration depth profiles for Ge (dashed-dotted), Mn (solid), and O (dashed) elements for as-implanted and annealed samples, respectively.

spectra are reported as a function of depth [panels (a) and (c)], as well as the corresponding atomic concentration depth profiles for Mn, Ge, and O elements [panels (b) and (d)]. In the as-implanted sample [Fig. 5(b)], the Mn concentration depth profile shows the quasi-Gaussian distribution typical of single-energy ion implantation processes, with a slight positive skewness. The projected range is about 55 nm, in perfect agreement with TRIM simulations, with a peak Mn atomic concentration of ~12%. Within the sensitivity of the technique, Mn atoms are revealed up to a depth of 120 nm, slightly below the thickness of the amorphized implanted layer (140 nm), as revealed by TEM measurements.

XPS spectra reveal the presence in the implanted layer of oxygen too. At the surface it has a concentration up to ~30%: its density rapidly decreases as a function of depth and completely disappears around 45 nm. Likely, these O atoms are adsorbed by the porous film due to exposure to air after the ion-implantation process, as it usually happens in porous semiconductors (see, for example, Ref. 55). The effect of oxygen on the chemical state of Mn atoms is clearly pointed out by the position and shape of the XPS Mn $2p_{3/2}$

spectrum [Fig. 5(a)]. A detailed study of the shape of this core level is out of the scope of this article, although some clear features can be stressed. At the surface, the Mn $2p_{3/2}$ line is peaked at a binding energy of about 642 eV, the chemical shift characteristic of MnO_2 oxide. Below the surface, a component peaked around 639 eV (corresponding to the Mn metallic state) appears and progressively increases at the expense of the oxidized one. Beginning from 45 nm, where oxygen disappears, the Mn $2p_{3/2}$ line is firmly centered at 638.7 eV; the same binding energy has been found for Mn diluted in GaAs both in neutral and singly negatively charged states.[56] The large asymmetry of the XPS line is due to multiplet splitting and other final state effects.[56] An oxidized Ge component is present only at the surface, as demonstrated by the shoulder around 32 eV (GeO_2), whereas below the surface only the component for pure material is found.

In Fig. 5(d) we report the XPS depth profiling analysis for the 400 °C annealed sample. A strong diffusion of Mn atoms, mainly towards the surface, occurs during the annealing at 400 °C. The preferential direction for diffusion is prob-
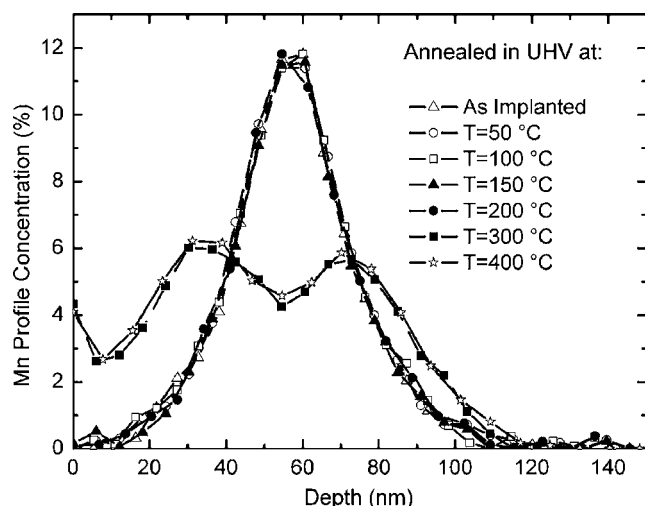
FIG. 6. Mn depth profiles as a function of annealing temperature: as-implanted, 50 °C, 100 °C, 150 °C, 200 °C, 300 °C, and 400 °C.
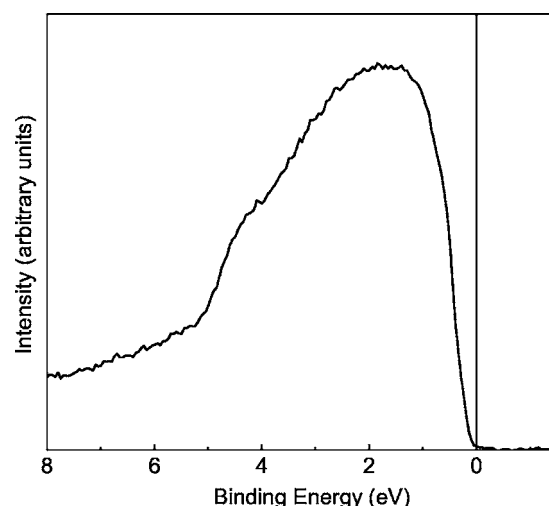

FIG. 7. Synchrotron radiation ($h\nu$=120 eV) angle-integrated valence band photoemission spectra for the 400 °C annealed sample after 60 nm Ar$^+$ sputtering. A linear background subtraction has been performed.

ably due to an increased mobility of Mn atoms in the porous surface layer. Accumulation of Mn around 30 nm below the surface gives rise to a peculiar two-peak distribution and it can be attributed to a gathering effect by oxygen atoms. However, a possible role of the Ge grain formation in diffusion of Mn atoms and their accumulation around 30 nm is debated in the Discussion.

A slight diffusion of O contaminants toward the bulk also occurs; however, no trace of oxygen is present below ~60 nm. As a matter of fact, also in this case, the Mn $2p_{3/2}$ XPS lines [Fig. 5(c)] show that in the first 55 nm a great part of Mn atoms is in an oxidized state, but at larger depth only the component centered at 638.7 eV, compatible with diluted Mn, is found.

The diffusion of Mn atoms has been studied in greater detail performing XPS depth profiles in samples annealed at temperature below 400 °C for the same time (60 min.), as shown in Fig. 6. The Mn profile remains unchanged up to 200 °C, but the annealing temperature of 300 °C is sufficient to establish a diffusion rate similar to that found at 400 °C. This is consistent with the fact that amorphous-to-polycrystalline Ge phase transition occurs in the range of annealing temperatures between 200 and 300 °C.

Figure 7 reports the angle-integrated valence band (VB) spectrum for the 400 °C annealed sample, obtained by soft x-ray synchrotron radiation. This spectrum has been taken after sputtering the external oxidized layer up to a depth where the O 1s core level signal was not detectable. This corresponds to a depth of about 60 nm inside the implanted layer [see Fig. 5(d)]. The spectrum shows negligible counts at the Fermi level (calibrated on the Ta clips of the sample holder) and a significant hump at 4.0 eV. These are undoubtedly spectroscopic signatures of Mn dilution in a crystalline Ge matrix.[34]

B. Magnetic properties

MOKE hysteresis loops relative to as-implanted and 400 °C annealed samples are shown in Fig. 8. They have been taken in polar geometry and in the temperature range 10–300 K. Similar results, but with worse signal-to-noise ratio, have been found in longitudinal geometry (not reported), inferring that the samples are magnetically isotropic. For both samples, the hysteresis loops have been collected in two different plots, corresponding to different temperature ranges, only for clarity. It is evident that the annealing treatment induces a great modification of the magnetic properties, which is obviously related to the change in the structural characteristics examined in the previous section.

The as-implanted alloy at 10 K shows a small coercive field (~350 Oe) and a relatively small remanence (~25% of saturation value); these two quantities rapidly decrease with temperature and disappear at 50 K. However, a strong S-shaped response continues to be evident up to about 150 K, with progressively smaller saturation. The hysteresis loops can be fitted through a phenomenological expression of the type

$$\theta(H) = \theta_S L[C(H \pm H_C)], \tag{1}$$

where θ is the MOKE polarization rotation as a function of the applied magnetic field H, θ_S is the saturation rotation, H_C is the coercive field, C is a constant proportional to the initial magnetic susceptibility, and L is the Langevin function

$$L(x) = \coth(x) - \frac{1}{x}. \tag{2}$$

The reliability and good quality of the fitting procedure is shown in panel (a) of Fig. 9 for the 10 K loop. The fact that the magnetic response can be reproduced using only one Langevin function suggests that a single structural component is responsible for the ferromagnetic behavior of the sample. Since no manganese oxide is ferromagnetic,[57] and the presence of Mn-Ge precipitates is excluded by x-ray- and electron-diffraction measurements, the ferromagnetic behavior of the sample up to ~20 K and the subsequent strong
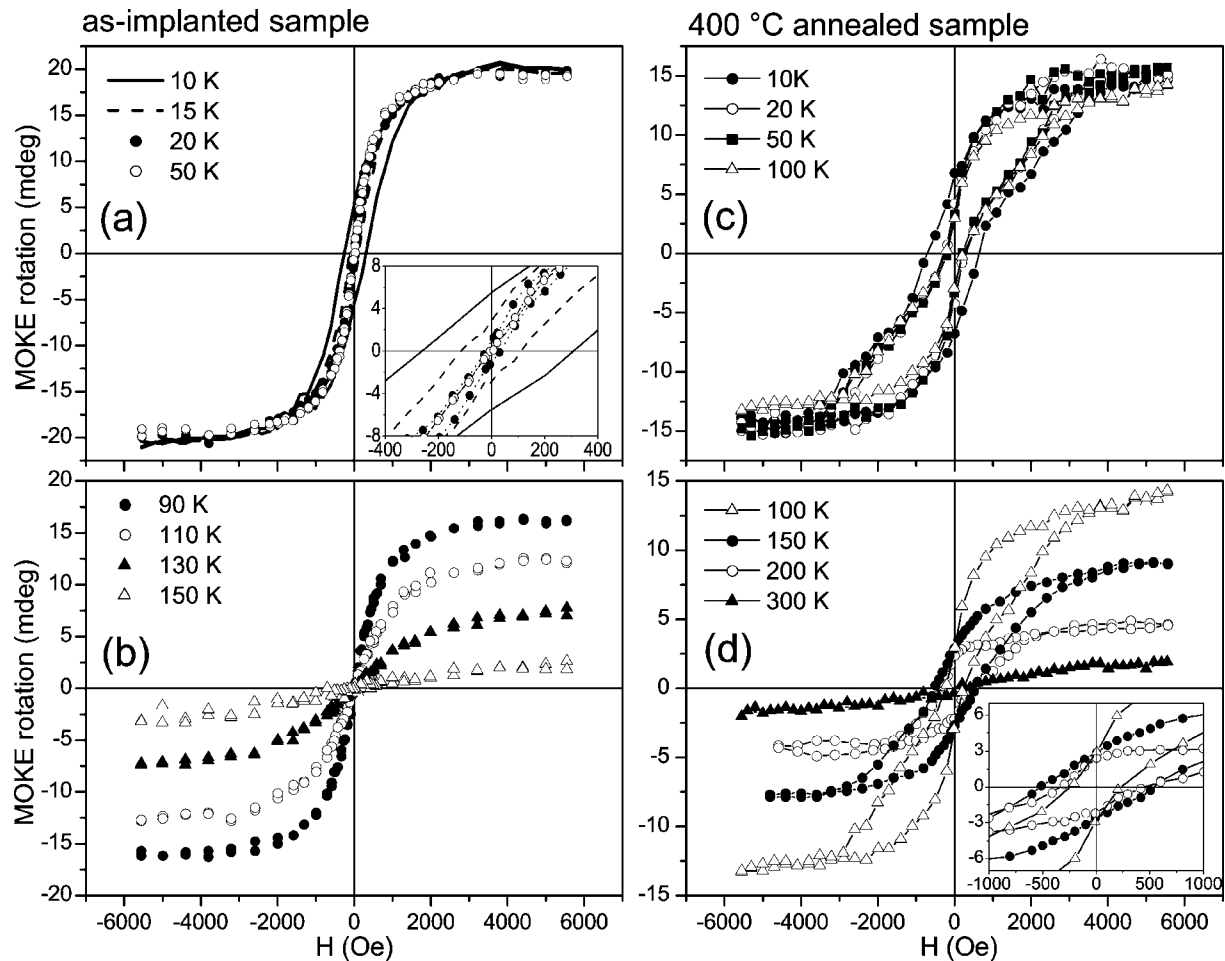
FIG. 8. On the left: MOKE hysteresis loops obtained in polar geometry for as-implanted sample in the ranges 10–50 K (a) and 90–150 K (b). The inset in (a) shows a magnification of hysteresis loops at low fields in the temperature range 10–50 K. On the right: MOKE hysteresis loops in polar geometry for the 400 °C annealed sample in the ranges 10–100 K (c) and 100–300 K (d). In the inset in (d) a magnification of the hysteresis loops at low fields for $T=100$, 150, and 200 K better illustrates the evolution of the coercive field with temperature.

nonlinear paramagnetic response must be ascribed to Mn atoms dispersed in the amorphous Ge implanted layer. Ferromagnetic properties in amorphous Mn_xGe_{1-x} samples, ascribed to a spin-glass transition, was found by Hauser[58] and Yu *et al.*,[59] although no proof of effective Mn dilution was given. The behavior of the fitting parameters H_C and M_S as a function of temperature is shown in Figs. 10(a) and 10(b), respectively (open squares in both cases). Our results for the as-implanted sample are very similar to those obtained on Mn_xGe_{1-x} amorphous films grown by deposition with similar values for the atomic concentration x,[59] where a coercive field of a few hundreds of Oe is found only at the lower temperatures, and a significant nonlinear behavior survives up to about 150 K.

As already pointed out, 400 °C annealing radically changes the magnetic response, as illustrated by the hysteresis loops shown in Figs. 8(c) and 8(d). Coercive field and remanence always have much greater values than in the as-implanted sample at the same temperatures, and the magnetic hysteresis continues to be present up to 250 K. The hysteresis loops in the range between 20 and 100 K present a low-field narrowing. This is verified by the anomalous behavior

of the coercive field as a function of temperature, shown in Fig. 10(a) (open circles). The experimental coercive field progressively decreases with T up to 100 K, but increases in the range 100–150 K, from ~200 Oe up to about 600 Oe [see the inset in Fig. 8(d)]. For higher temperatures, H_C decreases as a function of T, until it disappears completely around 300 K. The distorted shape of the hysteresis loops in the intermediate range of temperatures and the anomalous temperature dependence of the coercive field suggest that the magnetic response in the annealed sample is due to more than one structural component. Having in mind the cross-sectional TEM image of this sample [Fig. 3(c)], in a first hypothesis the presence of multiple magnetic contributions could be ascribed to the top 60 nm porous layer, and to the compact polycrystalline deeper region, respectively. However, in Fig. 10(a) we also report the experimental coercive field of the 400 °C annealed sample after the sputtering of the first 60 nm (open stars), already studied in valence-band photoemission measurements (Fig. 7). The behavior of H_C as a function of temperature is quite similar to that of the non-sputtered sample.
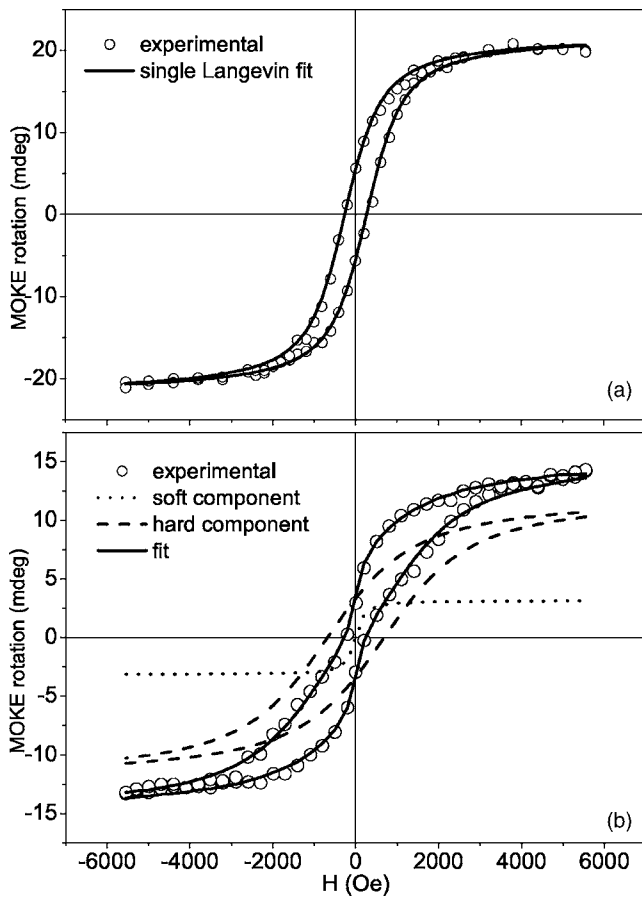
FIG. 9. Fitting of the MOKE hysteresis loops for (a) as-implanted sample at 10 K and (b) 400 °C annealed sample at 100 K. The hysteresis loop of the as-implanted sample is fitted with only one Langevin function [Eq. (1)], whereas for the annealed sample two Langevin functions, a hard component (dashed line) and a soft one (dotted line), are needed [see Eq. (3)].

This indicates that, actually, the layer between 60 and 140 nm is the only one responsible for the complex magnetic behavior and, therefore, a multiple magnetic contribution must be attributed to it. Actually, in the 60–140 nm deep region, two structural phases exist for the host Ge matrix: Ge nanocrystals and the surrounding amorphous Ge zones, both containing diluted Mn impurities.

Accordingly, we try to fit the hysteresis loops of the annealed sample as the sum of two magnetic components: a hard component, having a non-vanishing coercive field, and a soft component, with a paramagnetic behavior, whose coercive field is therefore set to zero. Using a Langevin function for each of the two components, hysteresis loops are fitted with the expression

$$\theta(H) = \theta_{SH} L[C_H(H \pm H_C^*)] + \theta_{SS} L[C_S H], \qquad (3)$$

where the parameters represent the extension of those in Eq. (1) for the hard and the soft component. H_C^* is the coercive field for the hard ferromagnetic component. Figure 9(b) shows an example of fitting for the hysteresis loop at 100 K. The two components are able to reproduce the experimental curves. In Fig. 10(a) we report the coercive field of the hard
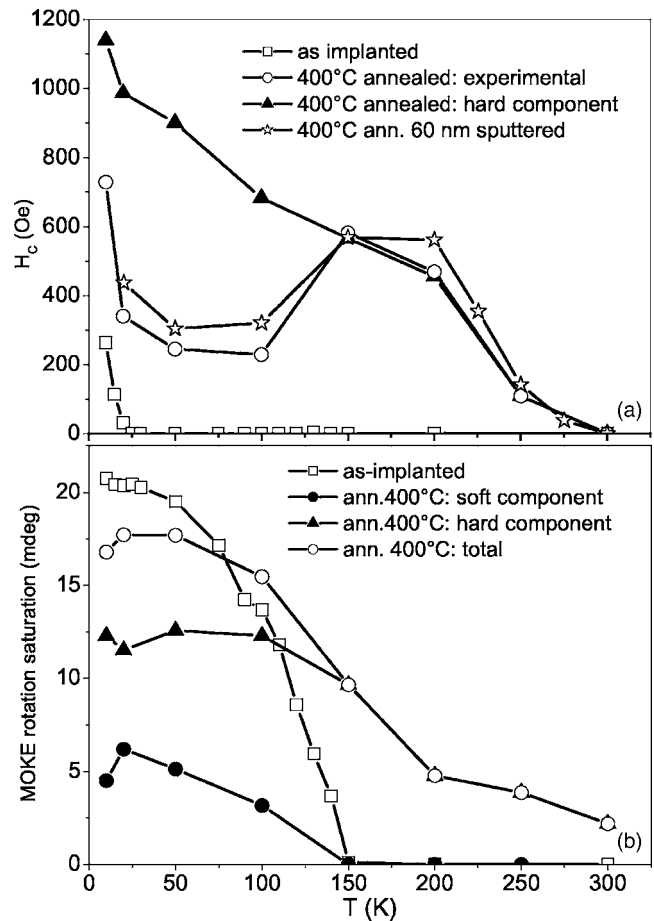

FIG. 10. (a) Coercive field as a function of temperature for the as-implanted sample (open squares), the 400 °C annealed sample (open circles), the 400 °C annealed sample after the sputtering of the first 60 nm (open stars), the hard component H_C^* in the 400 °C annealed sample [see Eq. (3)] (full triangles). (b) MOKE rotation saturation as a function of temperature for the as-implanted sample (open squares), the 400 °C annealed sample (open circles), and the contribution of its soft (full circles) and hard (full triangles) components.

component H_C^* as a function of T (full triangles). Differently from the experimental coercive field H_C, H_C^* monotonically decreases with T, as expected physically for a single magnetic component. For $T < 150$ K, H_C^* is always greater than H_C, the latter being reduced by the presence of the soft component, which has a more abrupt shape ($C_S > C_H$). Above 150 K, the hysteresis loop shape is more regular, and the coercive field of the ferromagnetic hard component H_C^* coincides to the overall experimental coercive field H_C. This clearly indicates that around 150 K the soft component disappears and the magnetic response is only due to the hard one. This is also verified by the temperature dependence of the MOKE rotation saturations for the hard component, θ_{SH} [full triangles in Fig. 10(b)] and the soft one, θ_{SS} (full circles in the same panel), obtained by the fitting procedure. In Fig. 10(b) we also show the sum of the two components (open circles) that constitutes the total MOKE rotation saturation. As expected from the comparison between H_C and H_C^*, the soft component completely disappears above 150 K and the

hysteresis loop can be well represented by the single hard-component Langevin function. Due to Mn atoms dispersed in amorphous Ge, the characteristics of the soft component are similar to those of the as-implanted sample. As the latter, it has a zero coercive field, except at low temperatures (10–15 K), and it also disappears at 150 K. Therefore, we can interpret the soft magnetic component in the 400 °C annealed sample as due to the diluted MnGe amorphous phase. On the contrary, the hard component can be attributed to the embedded diluted MnGe nanocrystals formed during the annealing process. In spite of the decreased Mn concentration due to the diffusion toward the surface, the dilution of Mn atoms inside the Ge nanocrystals leads to much more evident ferromagnetic properties in comparison with the dilution in amorphous Ge, and the magnetic hysteresis is evident up to 250 K, which can be assumed as the Curie temperature for our system. This Curie temperature is much greater than those [never exceeding ~120 K generally found in $Mn_x Ge_{1-x}$ single crystals with similar Mn atomic concentrations x (Refs. 17, 18, and 20).

IV. DISCUSSION

As already stressed in the Introduction, the fabrication of a good quality and effective diluted magnetic semiconductor is based on two different requests: (1) the presence of a sufficiently high concentration x of TM atoms in diluted phase, giving a Curie temperature T_C linearly increasing with x; (2) the presence of good crystalline quality in the host matrix, lattice defects being able to seriously affect the magnetic response, as well as the electrical properties, of the material. The structural information obtained on the room-temperature implanted MnGe alloys investigated in this work, if compared with the results on the 300 °C implanted samples,[34,35] clearly illustrates how it is hard to simultaneously satisfy these two demands, at least in the case of group-IV $Mn_x Ge_{1-x}$. In ion implantation, as well as in MBE and other growth techniques, the good crystalline quality of the processed layer is usually achieved by maintaining the substrate at a high temperature during the process (dynamical annealing effect). However, when dopants with very low solubility are introduced, as in the DMS fabrication, the thermally enhanced mobility of atoms, that has a fundamental role in the recombination of lattice damage, can also dramatically favor the precipitation of solute atoms and the formation of extrinsic phases. This detrimental effect of temperature has been verified both in ion-implanted[34,35] and in MBE-grown[10,36] MnGe samples, where it is possible to verify the formation of Mn-rich precipitates $(Mn_{11}Ge_8, Mn_5Ge_3)$ immersed in a Ge matrix with a quite perfect crystalline quality and containing an appreciable concentration of diluted Mn atoms. On the other hand, in this paper we show that a growth process at room temperature, due to the much lower atomic mobility of the two species (Mn and Ge), is effective in avoiding the precipitation of Mn atoms in extrinsic phases, but it is not able to preserve the crystalline order, the resulting implanted layer being completely amorphous. In spite of the very high peak concentration of diluted Mn atoms (~12%), a magnetic hysteresis is present only up to ~20 K,

as an effect of the absence of crystalline order. The use of intermediate temperature could not be the simple strategy to join high Mn dilution and crystalline perfection. As recently shown by Sugahara *et al.*,[20] the use of intermediate temperatures causes the formation of amorphous MnGe inclusions (with a Mn atomic concentration around 10–20 %). Thus, more sophisticated growth techniques could be requested to achieve effective dilution and efficient spin-polarized currents.

Contrarily to what could be expected, in our RT implanted sample, thermal annealing processes at 300–400 °C do not induce the precipitation of extrinsic MnGe phases together with the formation of Ge nanocrystals. Although Mn atoms appear to be diluted in the two amorphous and nanocrystalline Ge phases, the first structure giving very poor magnetic response, the annealed sample presents a magnetic hysteresis up to 250 K, much greater than the Curie temperatures found in MBE-grown $Mn_x Ge_{1-x}$ with similar x atomic concentration. We believe that this enhanced magnetic response, with respect to a bulk Ge DMS, has to be ascribed to a surface effect. The UHV annealing induces a growth of the Ge crystallites driven by the thermodynamical equilibrium. Accordingly, due to the low solubility of Mn impurities, the Ge polycrystalline reconstruction tends to exclude the substitutional incorporation of Mn atoms (which is obtained only with the use of out-of-equilibrium growth techniques). A great part of the Mn atoms in the Ge crystallites remain segregated at the crystallite facets where they find more energetically favored sites [as demonstrated through *ab initio* calculations by Profeta *et al.*[60] for the Ge(111) surface and by Zhu *et al.*[61] for the Ge(100) surface]. Indeed, Ge crystallites have an equilibrium crystal shape with a large fraction of (111) and (100) facets,[62] so the aforementioned grain boundary segregation is very likely. The same segregation mechanism probably plays an important role in the diffusion of Mn atoms observed upon annealing. Mn diffusion results activated after 300 °C annealing (see Fig. 6), and the formation of Ge nanocrystals, starts from that temperature (see Fig. 4). Moreover, although a gettering effect of O atoms cannot be excluded, after diffusion Mn impurities accumulate around 30 nm from the surface, which is the minimum depth at which Ge grains formed upon annealing.

The surface magnetism has been studied in particular for the Ge(111) surface in Ref. 60. There, Mn can occupy degenerate S_5, H_3, and surface interstitial sites. Mn in the former site (S_5) gives no magnetic contribution, whereas Mn interstitial or the H_3 site has a total magnetic moment of $3.2\mu_B$, slightly above the value of $3.0\mu_B$ found for substitutional Mn in the bulk.[15] This can favor segregation of Mn atoms at the facets of Ge crystallites, increasing the number of the surface-diluted magnetically active atoms. Thus, according to this proposed mechanism, a surface-enhanced magnetic response can be invoked to explain our observations for high Curie temperature in polycrystalline MnGe alloy.

A comparison of the magnetic response of these RT implanted samples with that obtained by high-temperature (300 °C) ion implantation[35] can be fruitful, reflecting the already discussed differences in the structural properties. The magnetic response of the RT as-implanted samples, where

Mn atoms are diluted into an amorphous Ge layer, presents analogies with the lower dose (1×10^{16} ions/cm^{-2}) 300 °C implanted sample, where only amorphous MnGe clusters are formed. Both samples present magnetic hysteresis only at the lower temperatures, but a nonlinear magnetic S-shaped response for a much wider temperature range. These similarities can be ascribed to the fact that the same magnetic phase (the amorphous MnGe alloy) is present in both samples, although in two very different distributions and shapes (a thin film in one case and nanosized particles in the other one). Presumably, in this case Mn atoms diluted in the Ge crystal do not play a pivotal role in determining the magnetic character of this high-temperature implanted sample. Instead, for 300 °C Mn$^+$ ion implantation at higher doses (2×10^{16} and 4×10^{16} ions/cm^{-2}), Curie temperatures T_C, not too far from room temperature, are found with a strong increase in the coercive field and remanence/saturation ratio. This improvement of the ferromagnetic properties cannot be simply ascribed to the greater amount of the incorporated Mn atoms, but, as already stressed in the Introduction, to the formation of precipitates with crystalline Mn$_5$Ge$_3$ structure. A short-range crystalline order, with a consequent enhancement of the ferromagnetic characteristics, is obtained in a RT implanted sample upon 400 °C UHV annealing, with the formation of polycrystalline Ge matrix with Mn atoms diluted in it. The improvement of ferromagnetic properties with respect to a proper Mn$_x$Ge$_{1-x}$ DMS is ascribed to an enrichment of Mn density on the surface of Ge polycrystals and not to a proper phase separation, as occurs in high-temperature implanted samples.

V. CONCLUSIONS

In summary, we have reported a detailed investigation of structural, electronic, and magnetic properties of Mn atoms diluted in a completely disordered phase (amorphous Ge) and in a phase with a short-range crystalline order (Ge nanocrystals). Room-temperature Mn ion implantation has been exploited to perform both amorphization and Mn doping of a Ge implanted layer (140-nm-thick). The amorphization process causes the roughening of the sample surface and is accompanied by the formation of a porous Ge film in the first 50–60 nm and by the relative adsorption of O contaminants. From diffraction measurements, no indication exists for the formation of crystalline MnGe precipitates. The Mn atoms, essentially diluted in the Ge amorphous layer, induce poor magnetic properties ($T_C \simeq 20$ K). 300 and 400 °C UHV annealing treatments allow the reconstruction of the amorphized implanted layer in randomly oriented Ge nanocrystals ($\sim$10 nm in diameter) with the presence of surviving amorphous regions, instead of an epitaxial regrowth from the crystalline substrate below. This phenomenon is accompanied by a strong diffusion of Mn dopants mainly toward the surface. A composite magnetic behavior results after annealing treatments. A proper fitting of the measured MOKE hysteresis loops has been interpreted in terms of two different magnetic components: a soft one, with a behavior similar to the magnetic response of the as-implanted layer—referable to Mn atoms diluted in the surviving amorphous regions—and a harder one that can be ascribed to a phase of diluted Mn in the Ge nanocrystals. The corresponding Curie temperature, higher than those usually found in MBE-grown monocrystalline Mn$_x$Ge$_{1-x}$, can be attributed to a segregation of Mn atoms at the surface of Ge nanocrystals, where their presence is energetically favored in specific lattice sites (interstitial and H$_3$). The high concentration of diluted and magnetically active Mn atoms on the nanocrystal surface is responsible for the enhanced magnetic properties with respect to monocrystalline Mn$_x$Ge$_{1-x}$.

*Electronic address: adriano.verna@aquila.infn.it

[1] H. Ohno, Science **281**, 951 (1998).

[2] S. A. Wolf, D. D. Awschalom, R. A. Buhrman, J. M. Daughton, S. von Molnr, M. L. Roukes, M. Y. Chtchelkanova, and D. M. Treger, Science **294**, 1488 (2001).

[3] G. A. Prinz, Science **282**, 1660 (1998).

[4] J. K. Furdyna, J. Appl. Phys. **64**, R29 (1988).

[5] Y. Ohno, D. K. Young, B. Beschoten, F. Matsukura, H. Ohno, and D. D. Awschalom, Nature (London) **402**, 790 (1999).

[6] H. Ohno, D. Chiba, S. Matsukura, T. Omiya, E. Abe, and T. Dietl, Nature (London) **408**, 944 (2000).

[7] S. Koshihara, A. Oiwa, M. Hirasawa, S. Katsumoto, Y. Iye, C. Urano, H. Takagi, and H. Munekata, Phys. Rev. Lett. **78**, 4617 (1997).

[8] *Semiconductors-Basic Data*, edited by O. Madelung (Springer-Verlag, Berlin, 1996).

[9] J. Shi, J. M. Kikkawa, R. Proksch, T. Schffer, D. D. Awschalom, G. Medeiros-Ribeiro, and P. M. Petroff, Nature (London) **377**, 707 (1995).

[10] Y. D. Park, A. Wilson, A. T. Hanbicki, J. E. Mattson, T. Ambrose, G. Spanos, and B. T. Jonker, Appl. Phys. Lett. **78**, 2739 (2001).

[11] A. H. MacDonald, P. Schiffer, and N. Samarth, Nat. Mater. **4**, 195 (2005), and references therein.

[12] A. M. Nazmul, T. Amemiya, Y. Shuto, S. Sugahara, and M. Tanaka, Phys. Rev. Lett. **95**, 017201 (2005).

[13] Y.-J. Zhao, T. Shishidou, and A. J. Freeman, Phys. Rev. Lett. **90**, 047204 (2003).

[14] T. Dietl, H. Ohno, F. Matsukura, J. Cibert, and D. Ferrand, Science **287**, 1019 (2000).

[15] A. Stroppa, S. Picozzi, A. Continenza, and A. J. Freeman, Phys. Rev. B **68**, 155203 (2003).

[16] H. H. Woodbury and W. W. Tyler, Phys. Rev. **100**, 659 (1955).

[17] Y. D. Park, A. T. Hanbicki, C. S. H. S. C. Erwin, J. M. Sullivan, J. E. Mattson, T. F. Ambrose, A. Wilson, G. Spanos, and B. T.

Jonker, Science **295**, 651 (2002).

[18] A. P. Li, J. Shen, J. R. Thompson, and H. H. Weitering, Appl. Phys. Lett. **86**, 152507 (2005).

[19] N. Pinto, L. Morresi, M. Ficcadenti, R. Murri, F. D'Orazio, F. Lucari, L. Boarino, and G. Amato, Phys. Rev. B **72**, 165203 (2005).

[20] S. Sugahara, K. L. Lee, S. Yada, and M. Tanaka, Jpn. J. Appl. Phys., Part 2 **44**, L1426 (2005).

[21] F. Tsui, L. He, A. Tkachuk, S. Vogt, and Y. S. Chu, Phys. Rev. B **69**, 081304(R) (2004).

[22] S. Choi, S. C. Hong, S. Cho, Y. Kim, J. B. Ketterson, C.-U. Jung, K. Rhie, B.-J. Kim, and Y. C. Kim, Appl. Phys. Lett. **81**, 3606 (2002).

[23] J.-S. Kang, G. Kim, S. C. Wi, S. S. Lee, S. Choi, S. Cho, S. W. Han, K. H. Kim, H. J. Song, H. J. Shin, A. Sekiyama, S. Kasai, S. Suga, and B. I. Min, Phys. Rev. Lett. **94**, 147202 (2005).

[24] M. A. Scarpulla, O. D. Dubon, K. M. Yu, O. Monteiro, M. R. Pillai, M. J. Aziz, and M. C. Ridgway, Appl. Phys. Lett. **82**, 1251 (2003).

[25] Y. Shon, W. C. Lee, Y. S. Park, Y. H. Kwon, S. J. Lee, K. J. Chung, H. S. Kim, D. Y. Kim, D. J. Fu, and T. W. Kang, Appl. Phys. Lett. **84**, 2310 (2004).

[26] V. A. Chitta, J. A. H. Coaquira, J. R. L. Fernandez, C. A. Duarte, J. R. Leite, D. Schikora, D. J. As, K. Lischka, and E. Abramof, Appl. Phys. Lett. **85**, 3777 (2004).

[27] M. H. Kane, A. Asghar, A. M. Payne, C. R. Vestal, Z. J. Zhang, M. Strassburg, J. Senawirante, N. Dletz, C. J. Summers, and I. T. Ferguson, Phys. Status Solidi C **2**, 2441 (2005).

[28] N. Theodoropoulou, A. F. Hebard, S. N. G. Chu, M. E. Overberg, C. R. Abernathy, S. J. Pearton, R. G. Wilson, and J. M. Zavada, J. Appl. Phys. **91**, 7499 (2002).

[29] S. J. Pearton, M. E. Overberg, G. T. Thaler, C. R. Abernathy, J. Kim, F. Ren, N. Theodoropoulou, A. F. Hebard, and Y. D. Park, Phys. Status Solidi A **195**, 222 (2003).

[30] A. F. Hebard, R. P. Rairigh, J. G. Kelly, S. J. Pearton, C. R. Abernathy, S. N. G. Chu, and R. G. Wilson, J. Phys. D **37**, 511 (2004), and references therein.

[31] M. Bolduc, C. Awo-Affouda, A. Stollenwerk, M. B. Huang, F. G. Ramos, G. Agnello, and V. P. LaBella, Phys. Rev. B **71**, 033302 (2005).

[32] L. Liu, N. Chen, Z. Yin, F. Yang, J. Zhou, and F. Zhang, J. Cryst. Growth **265**, 466 (2004).

[33] L. Liu, N. Chen, C. Chen, Y. Li, and Z. Y. F. Yang, J. Cryst. Growth **273**, 106 (2004).

[34] L. Ottaviano, M. Passacantando, S. Picozzi, A. Continenza, R. Gunnella, A. Verna, G. Bihlmayer, G. Impellizzeri, and F. Priolo, Appl. Phys. Lett. **88**, 061907 (2006).

[35] M. Passacantando, L. Ottaviano, F. D'Orazio, F. Lucari, M. De Biase, G. Impellizzeri, and F. Priolo, Phys. Rev. B **73**, 195207 (2006).

[36] C. J. C. Bihler, T. Vallaitis, M. Gjukic, M. S. Brandt, E. Pippel, J. Woltersdorf, and U. Gsele, Appl. Phys. Lett. **88**, 112506 (2006).

[37] S. Picozzi, L. Ottaviano, M. Passacantando, G. Profeta, A. Continenza, F. Priolo, M. Kim, and A. J. Freeman, Appl. Phys. Lett. **86**, 062501 (2005).

[38] M. J. Freiser, IEEE Trans. Magn. **MAG-4**, 152 (1968).

[39] J. F. Ziegler, J. P. Biersack, and U. Littmark, *The Stopping and Range of Ions in Solids* (Pergamon Press, New York, 1985).

[40] The etching rate has been estimated through comparison with a certified 1000 Å-thick SiO_2 thin film.

[41] R. Gunnella, L. Morresi, N. Pinto, R. Murri, L. Ottaviano, M. Passacantando, F. D'Orazio, and F. Lucari, Surf. Sci. **577**, 22 (2005).

[42] C. Quaresima, C. Ottaviani, M. Matteucci, C. Crotti, A. Antonini, M. Capozi, S. Rinaldi, M. Luce, P. Perfetti, K. C. Prince, C. Astaldi, M. Zacchigna, L. Romanzin, and A. Savoia, Nucl. Instrum. Methods Phys. Res. A **364**, 374 (1995).

[43] Y. J. Chen, I. H. Wilson, W. Y. Cheung, J. B. Xu, and S. P. Wong, J. Vac. Sci. Technol. B **15**, 809 (1997).

[44] S. O. Kucheyev, J. S. Williams, C. Jagadish, J. Zou, V. S. J. Craig, and G. Li, Appl. Phys. Lett. **77**, 1455 (2000).

[45] C. Ascheron, A. Schnidler, R. Flagmeyer, and G. Otto, Nucl. Instrum. Methods Phys. Res. B **36**, 163 (1989).

[46] R. Nipoti, E. Albertazzi, M. Bianconi, R. Lotti, G. Lulli, M. Cervera, and A. Carnera, Appl. Phys. Lett. **70**, 3425 (1997).

[47] W.-K. Chu, J. W. Mayer, and M.-A. Nicolet, *Backscattering Spectrometry* (Academic Press, New York, 1978).

[48] A. H. Clark, Phys. Rev. **154**, 750 (1967).

[49] B. Stritzker, R. G. Elliman, and J. Zou, Nucl. Instrum. Methods Phys. Res. B **175-177**, 193 (2001).

[50] S. M. Kluth, J. D. F. Gerald, and M. C. Ridgway, Appl. Phys. Lett. **86**, 131920 (2005).

[51] On the same cross-sectioned annealed sample, electron diffraction measurements performed on the monocrystalline Ge substrate (not shown) present no diffraction rings. This excludes that at the 130-nm-deep interface, polycrystalline rings are due to the TEM preparation.

[52] T. E. Haynes, M. J. Antonell, C. A. Lee, and K. S. Jones, Phys. Rev. B **51**, 7762 (1995).

[53] A. Guinier, *X-Ray Diffraction in Crystals, Imperfect Crystals and Amorphous Bodies* (W. H. Freeman & Co., San Francisco, 1963).

[54] The instrumental contribution to peak broadening has been estimated from the FWHM of the Si (111) diffraction peak ($2\theta = 28.44°$) of a monocrystalline Si wafer. Since it results in $\sim 0.04°$, instrumental contribution can be neglected.

[55] X. L. Wu, S. J. Xiong, D. L. Fan, Y. Gu, X. M. Bao, G. G. Siu, and M. J. Stokes, Phys. Rev. B **62**, R7759 (2000).

[56] J. Okabayashi, A. Kimura, O. Rader, T. Mizokawa, A. Fujimori, T. Hayashi, and M. Tanaka, Phys. Rev. B **58**, R4211 (1998).

[57] D. P. Norton, S. J. Pearton, A. F. Hebard, N. Theodoropoulou, L. A. Boatner, and R. J. Wilson, Appl. Phys. Lett. **82**, 239 (2003).

[58] J. J. Hauser, Phys. Rev. B **22**, 2554 (1980).

[59] S. S. Yu, T. T. L. Anh, Y. E. Ihm, D. Kim, H. Kim, S. Oh, C. S. Kim, and H. Ryu, Solid State Commun. **134**, 641 (2005).

[60] G. Profeta, S. Picozzi, A. Continenza, and C. Franchini, Phys. Rev. B **70**, 155307 (2004).

[61] W. Zhu, H. H. Weitering, E. G. Wang, E. Kaxiras, and Z. Zhang, Phys. Rev. Lett. **93**, 126102 (2004).

[62] A. A. Stekolnikov and F. Bechstedt, Phys. Rev. B **72**, 125326 (2005).